Catalytically Driven Colloidal Patterning and Transport

Timothy R. Kline,[†,‡] Jodi Iwata,[†] Paul E. Lammert,[‡,§] Thomas E. Mallouk,*[,†,‡,⊥] Ayusman Sen,*[,†,‡,⊥] and Darrell Velegol*[,‡,⊥,||]

Department of Chemistry, Center for Nanoscale Science, Department of Physics, Department of Chemical Engineering, and Materials Research Institute, The Pennsylvania State University, University Park, Pennsylvania 16802

Received: July 12, 2006; In Final Form: September 30, 2006

We recently reported the convection and pattern formation of tracers caused by a catalytically generated electric field. The electric field arises due to the heterogeneous electrochemical reduction and oxidation of hydrogen peroxide (H_2O_2) on silver (Ag) and gold (Au), respectively.[1] Here we describe an electrokinetic model, developed in conjunction with experiments, that explains the details of the convection and pattern formation phenomenon. The model also enables the measurement of reaction kinetic parameters that are otherwise difficult to obtain. This quantitative model serves as a platform for the modeling of other catalytic redox systems and systems with broken symmetries.

Introduction

The electrophoretic movement of individual colloidal particles due to an applied electric field has been studied for about two centuries, since the original observation by Reuss.[2] Several reviews describe electrokinetic theory and its fundamental results,[3−7] such as the Smoluchowski equation for electrophoresis. For particles with thin electrical double layers (EDLs), this equation gives the particle electrophoretic velocity ($\mathbf{U}_{ep}$)

$$\mathbf{U}_{ep} = \frac{\epsilon \zeta_p \mathbf{E}}{\eta} \tag{1}$$

in terms of the particle ζ potential (ζ_p, the electric potential at the particle surface relative to the bulk), the applied electric field ($\mathbf{E}$), and the fluid permittivity (ϵ) and viscosity (η).

The electrophoresis of particles is usually accompanied by an additional electroosmotic transport by the fluid. The particles move at their electrophoretic velocity given by eq 1, but they are also carried by the local fluid velocity ($\mathbf{v}$) that arises due to electroosmosis (i.e., $\mathbf{E}$ acting on the charged walls of the container or other nearby particles) and the resulting pressure-driven flows that result. These two electrokinetic effects (electrophoresis and electroosmosis) have been combined to give direct current (DC) electrophoretic deposition of particles into ordered arrays.[8,9] Reports also exist for AC ordering of particles,[10−14] but we restrict our attention to effects linear in $\mathbf{E}$. These ordered arrays of particles represent an advance from single particle movement to hierarchical assemblies of metastable colloidal crystallites. Formation of the hierarchical assembles does not require a lithographic mask, another technique previously used to generate hierarchical assembles. These mask-free hierarchical assembles result from an asymmetry in the system (i.e., a single particle adsorbed to the surface prior the electrophoretic deposition).[15]

Template-free patterning of particles was recently done in our lab, using a catalytic approach for generating metastable particle crystallites.[1] The experiments were inspired by previous observations of the autonomous movement of nanorods containing spatially defined catalytic zones (e.g., regions of gold and platinum).[16,17] In both cases the electrokinetic flows were produced by catalytic decomposition of H_2O_2.

$$H_2O_2 + 2H^+ + 2e^- \rightarrow 2H_2O \tag{2a}$$

$$H_2O_2 \rightarrow 2H^+ + 2e^- + O_2 \tag{2b}$$

$$2H_2O_2 \rightarrow 2H_2O + O_2 \tag{2c}$$

where, eq 2a is the reduction of H_2O_2 occurring on the silver; eq 2b is the oxidation of H_2O_2 occurring on the gold; and eq 2c is the sum of the two half-reactions often referred to as the disproportionation of H_2O_2 to O_2 and H_2O.

The purposes of this paper are several. First, we provide a detailed electrokinetic model that explains the observed particle movement for the geometry shown in Figure 1. The modeling procedure can be applied to other catalytically generated electrokinetic flows, such as that described by Paxton et al. in the electrochemical decomposition pathway for platinum/gold-interdigitated microelectrodes in H_2O_2.[18] Second, we show good agreement between observed particle movement and the model. Finally, we show how by combining modeling and experiment, we are able to measure reaction kinetic parameters that were previously very difficult to obtain. The model is sufficiently predictive that it will be used to design template-free patterning and flows given other surface geometries, thus providing a way of treating "surfaces as motors".

Experimental Methods

Tracer Synthesis. We used tracers consisting of gold nanorods synthesized by bulk electrolysis from metal salt solutions into pores of anodized alumina membranes coated with

* Address correspondence to these authors. E-mail: velegol@psu.edu, asen@chem.psu.edu, tom@chem.psu.edu.
[†] Department of Chemistry.
[‡] Center for Nanoscale Science.
[§] Department of Physics.
[⊥] Materials Research Institute.
[||] Department of Chemical Engineering.

10.1021/jp064393l CCC: $33.50
Published on Web 11/11/2006

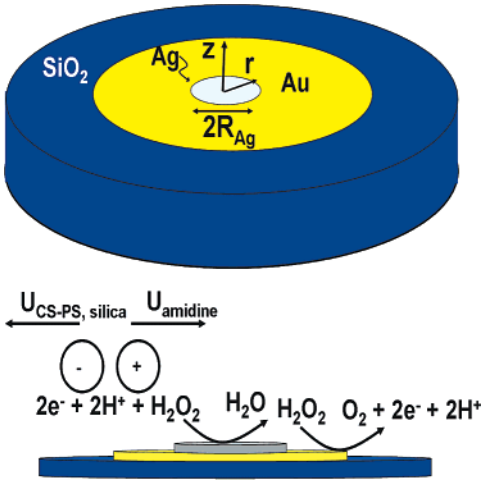

Figure 1. Schematic of the catalytic surface. The inner disk is silver, and it is surrounded first by an electrically connected larger gold disk, and then by glass (SiO_2) in the outermost region. We vary the radii (R) of the three regions, and we examine the movement of tracer particles in aqueous H_2O_2 solutions, due to the electrochemical decomposition of H_2O_2 over the catalysts. Negatively charged silica particles and carboxyl or sulfate polystyrene latex (PSL) particles form a ring pattern over the gold. Positively charged amidine PSL particles convect inward toward silver with a velocity $U_{amidine}$.

silver as described previously.[19,20] Briefly, 200 nm of silver was sputtered onto anodized alumina membranes (Whatman) which function as the working electrode in an electrochemical cell. Then metals are deposited into the pores of the template (~400 nm) to create cylindrical nanostructures. All other tracers employed were available commercially, polystyrene microspheres (both negatively and positively charged) and silica spheres. Spheres were 1−3 μm in diameter. Negative polystyrene microspheres were obtained from Polysciences, positive polystyrene from Interfacial Dynamics, and silica microspheres from Bangs Labs.

In the SAM-modified gold nanorods, monolayer stability was confirmed by using a combination of ellipsometry and X-ray photoelectron spectroscopy (XPS) where XPS also served to identify changes in the monolayer from the strongly oxidizing H_2O_2 (see the Supporting Information for XPS spectra of the S 2p region of MESA modified surfaces before and after H_2O_2 exposure). The monolayer remained intact and in fact did not appear chemically different, although curve fitting suggested possible compositional changes.

Surface Fabrication. Conventional microfabrication was employed to build the surfaces. Briefly, a photomask was designed on LEDIT and then written on a Heidelberg Laser Writer on a soda lime 4 in. mask. The mask was used in conventional photolithography to transfer patterns onto photoresist/lift-off resist (Shipley SPR3012/Microchem LOR-5A) coated 3 in. silicon wafers containing a 0.9 μm layer of thermally grown oxide (SiO_2). After a 6 s exposure (365 nm wavelength) and pattern development in 0.26 N tetramethylammonium hydroxide (Rohm and Haas CD-26) 10 nm of chromium followed by 100 nm of gold was deposited by physical vapor deposition (Lesker evaporator). Photoresist and lift-off resist were removed with acetone and CD-26 respectively to leave behind structures. A second layer of lithography and subsequent PVD was then employed to pattern the silver (150 nm) on the gold disks.

Motility Studies. In a typical fluid pumping experiment, an adhesive gasket (8 mm in diameter, Molecular Probes) was mounted onto the silver/gold containing oxidized Si wafer to minimize hydrodynamic flows. Then 10 μL of 1% w/w H_2O_2 was mixed with 10 μL of an aqueous suspension of one of the tracers, dispensed into the gasket, capped with a cover slide, and placed under a microscope (Olympus 60BXE) to observe particle behavior. Videos were then captured with MGI Videowave software at 10 frames per second, unless otherwise noted. Video feeds were analyzed to obtain trajectory plots with PhysVis (Kenyon college).

Kinetic Measurements. Electric field measurements were done on surfaces as synthesized above, but now two macroscopic gold electrodes were deposited onto the surface with the use of a shadow evaporation technique (i.e., aluminum foil protects silver/gold features and some surrounding SiO_2 area while all else is coated with gold). The electrodes were wired with insulated wires connected to a Keithley 2600 sourcemeter from which voltages were applied and currents measured. Bulk solution conductivity was measured immediately before the experiment. The applied voltage was ramped at 0.1 V steps until either patterning or convection was perturbed for negatively or positively charged tracers, respectively.

Results and Discussion

Electrokinetic Modeling. In principle, the particle velocities are modeled by solving simultaneously the coupled partial differential equations for the ion flux, the electric fields, the flow fields, and the particle motions. In practice, we will solve for these pieces separately with knowledge of the pertinent physics. We break the observed particle velocity ($\mathbf{U}$) into three parts: the electrophoretic velocity ($\mathbf{U}_{ep}$), the electroosmotic part ($\mathbf{v}_{eo}$) due to bulk fluid motion, and the net gravitational settling velocity ($\mathbf{U}_g$):

$$\mathbf{U} = \mathbf{U}_{ep} + \mathbf{v}_{eo} + \mathbf{U}_g \tag{3}$$

Several assumptions are made in the model, and we justify the most significant ones here. First, we use the electrophoretic velocity as given by the Smoluchowski equation (eq 1). Given that our Debye lengths (κ^{-1}) are typically about 180 nm (equilibrium water has dissolved CO_2, which gives carbonic acid; the resulting pH of 5.5 or 5.6 gives an ionic strength of about 2.8 μM), while our particle radii (a) are ~2 μm, an O'Brien and White analysis[4] reveals that eq 1 predicts a particle velocity about 40% too high. However, the use of the Smoluchowski equation gives a representative value, and if needed, more exact calculations could be done for spheres, soft spheres, cylinders, or other particles. In addition, the use of eq 1 means that we neglect any change in the electrophoretic velocity due to wall effects. For expected distances between the particle and wall due to colloidal forces, an analysis reveals a negligible error due to wall effects.[21]

Another assumption we make is that $\mathbf{v} \approx \mathbf{v}_{eo}$ in the region where we observe the particles. The fluid velocity ($\mathbf{v}_{eo}$) in the cell depends upon the electroosmotic velocity at the fluid cell walls, and also upon the pressure-driven terms arising from these flows. For infinitesimal EDLs the surface electroosmotic velocity is given by

$$\mathbf{v}_{eo} = -\frac{\epsilon \zeta_w \mathbf{E}}{\eta} \tag{4}$$

where the wall ζ potential is ζ_w. The pressure gradients are small from the equation of motion, because we know that the pressure field in the radial direction scales as $p_0 = \eta \mathbf{v}_{eo}/R_{Au}$. This pressure drives a flow in the radial direction of order $\mathbf{v}_r(z) \approx z\mathbf{v}_{eo}/R_{Au}$. If $z < 3$ μm and $R_{Au} = 35$ μm or more, then the pressure-driven

contribution near the wall is small. Thus, since our particles are close to the wall, we make the assumption that $\mathbf{v} \approx \mathbf{v}_{eo}$.

With these assumptions, both the radial electrophoretic and electroosmotic velocities depend on the electric field (**E**) in the solution. Using a matched expansion, we solve for the **E** field. Then to obtain the *z* direction particle velocity, we employ the fluid continuity equation.

Inner Solution for the E Field. In a static situation (i.e., no chemical reaction), an electrical double layer arises, and the potential drop across the double layer follows the Gouy−Chapman theory, which is solved based on the Poisson−Boltzmann equation.[22] Our system is not at equilibrium (i.e., a chemical reaction is occurring), and so we cannot use the Boltzmann distribution for ion concentration (n_i, in #/m^3) of species *i*. Instead we begin with the Nernst−Planck equation for the flux ($\mathbf{J}_i$, in units #/m^2·s) of ion *i*:

$$\mathbf{J}_i = -D_i \nabla n_i + z_i e n_i \mathbf{E} \mu_i + \mathbf{v} n_i \tag{5}$$

where D_i is the diffusion coefficient of ion type *i* (units m^2/s), z_i is its valence, $\mu_i = D_i/kT$ is its mobility (kT is the thermal energy), *e* is the proton charge (1.6×10^{-19} C), **E** is the electric field (units V/m), and **v** is the fluid velocity.

For the common case when $E > 6\pi\eta a\mathbf{v}/Ze$ (~0.1 V/cm for most atoms), one finds that the convective term in the Nernst−Planck equation is negligible, and thus one can obtain the electric field uncoupled from the velocity field. Neglecting the convective term is ordinarily assumed in similar electrokinetic problems, and we will make this assumption in our analysis. Our electric fields are usually greater than 1 V/cm. Furthermore, we believe that neglecting the convective term is particularly true for H^+ ions (or $H_9O_4^+$, since H^+ is likely solvated by water molecules), since H^+ has a high diffusion constant due to the Grotthus mechanism. For static electric fields we define an electrical potential (ψ) by $\mathbf{E} = -\nabla\psi$ to obtain

$$\mathbf{J}_i = -D_i \nabla n_i - \frac{z_i e D_i n_i}{kT} \nabla\psi \tag{6}$$

The ion flux equation is supplemented by the Poisson equation of electrostatics:

$$\nabla^2\psi = \frac{-\rho_f}{\epsilon} = \frac{-\sum_i z_i e n_i}{\epsilon} \tag{7}$$

where ρ_f is the free charge density in the solution (units C/m^3) and ϵ is the fluid permittivity (units C^2/N·m^2). We will analyze the case of a symmetric electrolyte with $Z = z^+ = z^- = 1$, so that $Ze = e$.

The other assumptions we made in calculating the inner solution are as follows: (1) the system is at steady state (time independent), (2) only monovalent electrolytes exist, and (3) fluxes near the surface are in the *z* (vertical) direction only ($\mathbf{J}_i = J_i\mathbf{i}_z$ and $\mathbf{E} = E\mathbf{i}_z$ in the EDL). We nondimensionalize eqs 6 and 7 using $\phi = e\psi/kT$, $c_i = n_i/n_0$, $j_i = J_i\kappa^{-1}/D_i n_0$, $\nabla = \kappa^{-1}\nabla$, and $y = \kappa z$. The term ∇ is a nondimensional gradient operator. Typical scales are for potential 25 mV, for distance the Debye screening length 180 nm (pH 5.5 equilibrium water, where $H^+ = 3.2 \times 10^{-6}$ M $= 1.90 \times 10^{21}$ per m^3), and for the electric field 25 mV/178 nm = 1400 V/cm. The scale for flux depends upon $D_+ = 9 \times 10^{-9}$ m^2/s for H^+, the concentration, and the Debye length; its scale is 9.6×10^{19} per m^2·s. The nondimensionalization gives

$$\mathbf{j}_+ = -\nabla\hat{c}_+ - c_+\nabla\hat{\phi} \tag{8}$$

$$\mathbf{j}_- = -\nabla\hat{c}_- + c_+\nabla\hat{\phi} \tag{9}$$

$$\nabla^2\hat{\phi} = -\frac{1}{2}(c_+ - c_-) \tag{10}$$

Since $\mathbf{j}_- = 0$ for both the unperturbed and perturbed cases, eq 9 merely says that the negative ion is distributed according to the Boltzmann distribution. Thus $c_- = \exp(\phi)$. Similarly, for the unperturbed case, $c_+ = \exp(-\phi)$. Equation 10 is obtained since for the unperturbed case, the Debye parameter comes from $\kappa^2 = 2Z^2e^2n_0/\epsilon kT$.

The final starting equation we need, before applying the boundary conditions, is conservation of ions. In the conservation of ions, we assume steady-state conditions, $\nabla\cdot\mathbf{J}_i = 0$. This means that in the EDL the net $\mathbf{J}_i = 0$. In nondimensional form, the conservation equation becomes

$$\nabla\cdot\mathbf{j}_i = 0 \tag{11}$$

We will do a perturbation analysis, because the reaction causes only small changes to the system. We will let "0" be the nonreaction case, and "1" be the change due to the reaction. The perturbation scheme applies as long as the "1" terms are much smaller than the "0" terms. Then we will ignore terms second order in smallness later.

$$\phi = \phi_0 + \phi_1 \tag{12}$$

$$c_+ = c_0^+ + c_1^+ \tag{13}$$

$$c_- = c_0^- + c_1^- \tag{14}$$

For the inner problem the only significant changes are in the *z* direction (*y* nondimensional), giving

$$\frac{d^2\phi}{dy^2} = -\frac{1}{2}(c_+ - c_-) \tag{15}$$

$$j_+ = -\frac{dc_+}{dy} - c_+\frac{d\phi}{dy} \tag{16}$$

$$j_- = -\frac{dc_-}{dy} + c_-\frac{d\phi}{dy} \tag{17}$$

The boundary conditions are that on a surface S_α (where α might be for silver, gold, or glass),

$$\phi = \phi_\alpha$$

$$j_+ = j_\alpha$$

$$j_- = 0 \tag{18}$$

For *y* approaching infinity (which again, on the length scale of *h* is still very near the surface)

$$-\nabla\hat{\phi} \rightarrow \hat{E}$$

$$c_+ \rightarrow 1$$

$$c_- \rightarrow 1 \tag{19}$$

Plugging in these values gives us the leading order terms and the perturbations as

$$\frac{d^2\phi_0}{dy^2} = -\frac{1}{2}(c_+^0 - c_-^0), \frac{d^2\phi_1}{dy^2} = -\frac{1}{2}(c_+^1 - c_-^1) \quad (20)$$

$$0 = -\frac{dc_0^+}{dy} - c_0^+\frac{d\phi_0}{dy}, j_\alpha = -\frac{dc_1^+}{dy} - c_1^+\frac{d\phi_0}{dy} - c_0^+\frac{d\phi_1}{dy} \quad (21)$$

$$0 = -\frac{dc_0^-}{dy} + c_0^-\frac{d\phi_0}{dy}, 0 = -\frac{dc_1^-}{dy} + c_1^-\frac{d\phi_0}{dy} + c_0^-\frac{d\phi_1}{dy} \quad (22)$$

Out of these we find

$$c_0^+ = \exp(-\phi_0), c_0^- = \exp(+\phi_0), \phi_0 \approx \phi_\alpha \exp(-y) \quad (23)$$

The approximate sign for potential is if we allow small potentials (Debye−Huckel). Allowing small potentials is unnecessary; we could use the full Gouy−Chapman result, which gives an exponential decay with y. Substituting gives

$$c_0^+ = \exp[-\phi_\alpha \exp(-y)], c_0^- = \exp[+\phi_\alpha \exp(-y)] \quad (24)$$

We now define a nondimensional electric field

$$\hat{E} \equiv \frac{E_z e}{kT\kappa} = -\frac{d\phi}{dy} \quad (25)$$

that gives

$$j_\alpha = -\frac{dc_1^+}{dy} + c_1^+\phi_\alpha \exp(-y) + \exp[-\phi_\alpha \exp(-y)]\hat{E} \quad (26)$$

We want the limit of this expression as $y \rightarrow \infty$ (but still small when viewed on the length scale of h). The limit as $y \rightarrow \infty$ is

$$j_\alpha = -\frac{dc_1^+}{dy} + \hat{E} \quad (27)$$

Similarly,

$$0 = -\frac{dc_1^-}{dy} - \hat{E} \quad (28)$$

But we also know that

$$\frac{d^2\phi_1}{dy^2} = -\frac{d\hat{E}}{dy} = -\frac{1}{2}(c_1^+ - c_1^-) \quad (29)$$

We expect that $\hat{E}$ will approach a constant value (giving electroneutrality outside the double layer), and so the solution to these equations for $y \rightarrow \infty$ is

$$c_1^+ = c_2^+, 2\hat{E} \rightarrow j_\alpha \quad (30)$$

The resulting concentration gradients can be calculated as perturbations to the original concentration fields.

In our derivation we assumed that the surface potential (ψ_{Au}) over the entire Au surface is uniform, as is the surface potential over the entire silver surface (ψ_{Ag}), and that both surface potentials arise not from flowing electrons (which would give a negligible potential), but for instance from adsorbed species. We have also assumed that the surface potentials do not change when a reaction occurs, which is not quite true.[23] Thus our final solution to the inner problem is given by

$$E_z = \begin{cases} \dfrac{J_{Ag}kT}{2eD_+n_0} & r \le R_{Ag} \\ \dfrac{J_{Au}kT}{2eD_+n_0} & R_{Ag} < r \le R_{Au} \\ 0 & R_{Au} < r \end{cases} \quad (31)$$

This is similar to Bard's eq 4.2.1 in ref 24, which was derived in a simple way by neglecting the diffusive term in eq 6 and solving for the electric field. However, by including the diffusive flux near the surface, one obtains an extra factor of 2.

Since the entire system must be electroneutral, the reaction rates on the gold and silver are related. Per unit area, gold is the rate-limiting catalyst; however, its area is typically larger. We choose the simplest model for relating the reaction rates, and therefore electric fields. We assume that for sufficiently large gold area, the silver reaction rate is at its maximum, and that the gold rate is at its maximum; thus, the maximum effective size of the gold ($R_{Au,max}$) is usually smaller than the actual size (R_{Au}). Furthermore, we have assumed that the reaction rates (J_α) are uniform over either the gold surface or the silver surface. These assumptions give

$$E_{Ag} = -\frac{R_{Au,max}^2 - R_{Ag}^2}{R_{Ag}^2}E_{Au} \quad (32)$$

More complicated models relating these reaction rates have been tried, and while they change the quantitative results slightly, they do not change the qualitative results compared with eq 32.

Outer Solution for the E Field. By knowing the inner **E** field from the catalytic reactions occurring on the surface, we can solve for the **E** field in the "outer region", where the particle resides. In calculating the outer solution we identified the equivalent surface charge density that gives the **E** field found for the inner solution. A well-known result is that planar surfaces possessing uniform surface charge density (ρ_s) have a vertical electric field $E_z = \rho_s/\epsilon$ (since the field lines go only upward).[25] On silver, gold, or glass for our situation, we can thus give an equivalent surface charge density

$$\rho_\alpha/\epsilon = E_\alpha \quad (33)$$

where E_α is given by eq 31. Given an arbitrary surface charge density (ρ_s), one can find the resulting electric field as[25]

$$\mathbf{E}(\mathbf{x}) = \frac{1}{4\pi}\int\int_S \frac{\rho_s \cdot (\mathbf{x} - \mathbf{x}')}{\epsilon|\mathbf{x} - \mathbf{x}'|^3}\,dS' \quad (34)$$

Combining eqs 33 and 34 gives the following expression for the electric field in the "outer region":

$$\mathbf{E}(\mathbf{x}) = \frac{1}{4\pi}\int\int_S \frac{E_\alpha \cdot (\mathbf{x} - \mathbf{x}')}{|\mathbf{x} - \mathbf{x}'|^3}\,dS' \quad (35)$$

Our geometry consists of three concentric circles as described by eq 31. We will assume that they each have a uniform ζ potential and reaction rate as defined by eq 32. We define the pertinent vector quantities in cylindrical coordinates:

$$\mathbf{x} = z\mathbf{i}_z + r\mathbf{i}_r$$

$$\mathbf{x}' = 0\mathbf{i}_z + r'\mathbf{i}'_r$$

$$\mathbf{x} - \mathbf{x}' = z\mathbf{i}_z + r\mathbf{i}_r - r'\mathbf{i}'_r$$

$$|\mathbf{x} - \mathbf{x}'| = [(z\mathbf{i}_z + r\mathbf{i}_r - r'\mathbf{i}'_r)\cdot(z\mathbf{i}_z + r\mathbf{i}_r - r'\mathbf{i}'_r)]^{1/2} \quad (36)$$

The unprimed geometric variables are for the location where we desire to know the field (point of observation), while the primed variables are dummy variables over which we will do the integrations. In cylindrical coordinates we have $\mathbf{i}_r = \cos\theta\mathbf{i}_x + \sin\theta\mathbf{i}_y$, and so

$$|\mathbf{x} - \mathbf{x}'| = (z^2 + r^2 + r'^2 - 2rr'\sin\theta\sin\theta' - 2rr'\cos\theta\cos\theta')^{1/2} \quad (37)$$

$$\mathbf{E}(\mathbf{x}) = \frac{1}{4\pi}\int_0^{2\pi}\int_0^{\infty}\frac{E_\alpha\cdot(\mathbf{x}-\mathbf{x}')}{|\mathbf{x}-\mathbf{x}'|^3}r'\,dr'\,d\theta' = \frac{1}{4\pi}\int_0^{2\pi}\int_0^{\infty}\times \frac{E_\alpha\cdot(z\mathbf{i}_z + r\mathbf{i}_r - r'\mathbf{i}'_r)}{(z^2 + r^2 + r'^2 - 2rr'\sin\theta\sin\theta' - 2rr'\cos\theta\cos\theta')^{3/2}}r'\,dr'\,d\theta' = \frac{1}{4\pi}\int_0^{2\pi}\int_0^{\infty}\times \frac{E_\alpha\cdot(z\mathbf{i}_z + r\cos\theta\mathbf{i}_x + r\sin\theta\mathbf{i}_y - r'\cos\theta'\mathbf{i}_x - r'\sin\theta'\mathbf{i}_y)}{(z^2 + r^2 + r'^2 - 2rr'\sin\theta\sin\theta' - 2rr'\cos\theta\cos\theta')^{3/2}}r'\,dr'\,d\theta' \quad (38)$$

This equation gives the electric field for the "outer region", subject to the assumptions listed earlier. Of course, the **E** field is radially symmetric, and so we can choose any θ; that is, the **E** field in the $\mathbf{i}_x$ direction is the same for $\mathbf{i}_y$ or any $\mathbf{i}_r$. We choose $\theta = 0$. In addition, we define $s = r/R_{Ag}$, $s' = r'/R_{Ag}$, and $w = z/R_{Ag}$. Now

$$\mathbf{E}(r,z) = \frac{E_{Ag}}{4\pi}\int_0^{2\pi}\int_0^{1}\times \frac{w\mathbf{i}_z + (s - s'\cos\theta')\mathbf{i}_r}{(w^2 + s^2 + s'^2 - 2ss'\cos\theta')^{3/2}}s'\,ds'\,d\theta' + \frac{E_{Au}}{4\pi}\int_0^{2\pi}\int_1^{R_{Au,max}/R_{Ag_s}}\frac{w\mathbf{i}_z + (s - s'\cos\theta')\mathbf{i}_r}{(w^2 + s^2 + s'^2 - 2ss'\cos\theta')^{3/2}}s'\,ds'\,d\theta' \quad (39)$$

Particle Velocities Obtained from the *E* Field. The calculated electric field must in the end be used to calculate the particle velocity. In the radial (r) direction, we have already established in eq 3 that $\mathbf{U} = \mathbf{U}_{ep} + \mathbf{v}_{eo}$, since we assume that the particle is close to the surface (on the length scale h) and mostly unaffected by the bulk flow in the cell. At the same time we have assumed that the particle is far enough from the wall (on the length scale of the particle size a) that we do not need to consider surface interactions. Both assumptions can be accounted for, but in this paper they will be neglected. We will also ignore nonuniform electric fields acting on the particles, which is more important for the case of rod-shaped or disk-shaped particles than for spheres.[26] Thus,

$$U_r = \frac{\epsilon(\zeta_p - \zeta_w)E_r}{\eta} \quad (40)$$

The application of eqs 39 and 40, which can be integrated easily on for instance Mathematica software, gives the *radial* velocity as shown in the lower part of Figure 2.

The next step is to calculate the z component of **U**. *Near the surface*, the radial velocity varies little in the z direction, but varies more in the r direction. Therefore, we use the fluid continuity equation to obtain v_z of the fluid. Coupled with the electrophoretic motion, v_z gives the particle velocity as

$$U_z = \frac{\epsilon\zeta_p E_z}{\eta} + v_z + U_g \quad (41)$$

where again E_z is obtained from eq 39. U_g is due to the settling caused by gravity, which is small for many polymer colloids (since the density difference $\rho_p - \rho_f$ between the particle and fluid is small), but which can be significant for gold particles. The inclusion of gravity is readily obtained for spheres since $U_g = 2a^2(\rho_p - \rho_f)g/9\eta$, but we will not include it further in our analysis. We note that particles like gold, which settle more quickly, will still not touch the surface, due to repulsive electrostatic colloidal forces.

The fluid continuity equation is

$$\frac{\partial v_z}{\partial z} + \frac{1}{r}\frac{\partial}{\partial r}(rv_r) = 0 \quad (42)$$

Integrating this equation gives

$$v_z(z) = -\int_0^z \frac{1}{r}\frac{\partial}{\partial r}(rv_r)\,dz' \quad (43)$$

since $v_z = 0$ at $z = 0$ (the electroosmotic velocity is radial). The integral for v_z can again be done relatively easily on Mathematica software.

Figure 2 shows a vector plot of the electric field and tracer velocity for the system later described in Figure 3. There are several important points. The electric field, overall, behaves as a dipole field. At a critical radius (r_{crit}) from the center, the radial electric field becomes zero, and for larger r it then changes direction. The band of tracers forms where $r = r_{crit}$, and as the tracers continue to approach the band region, a 2-D colloidal crystal often forms (Figure 4). The point r_{crit} where $E_r = 0$ depends only weakly on the ratio $R_{Au,max}/R_{Ag}$, where $R_{Au,max}$ is the maximum radius of gold disk that makes any significant catalytic contribution. We find that the maximum E_r over the gold occurs where $r = R_{Au,max}$, which we have usually found to be 36 μm (72 μm gold diameter) for a 20 μm silver disk

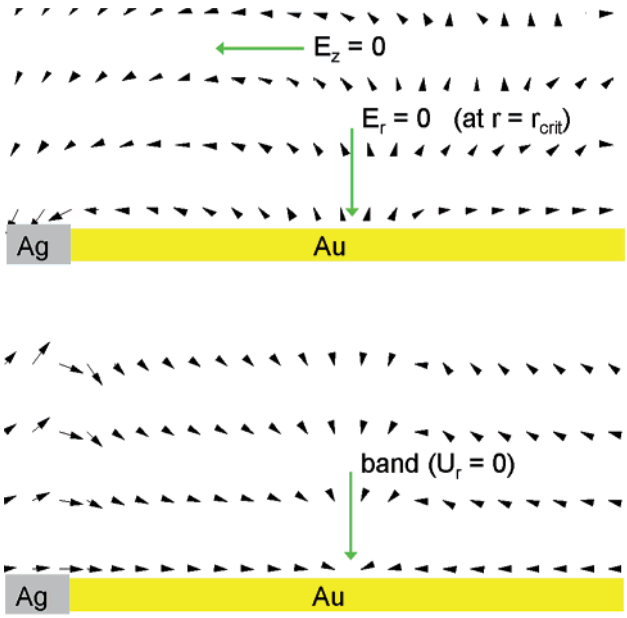

Figure 2. Model prediction showing a vector plot of the electric field (top) and particle velocities (bottom) for the system. The silver and gold surfaces are shown in the figure; the glass is outside of the region of interest. The lower left represents $r = 6$ μm from the center of the silver disk (i.e., not all the silver is shown) and $z = 0$, while the upper right represents $r = 60$ μm and $z = 20$ μm.

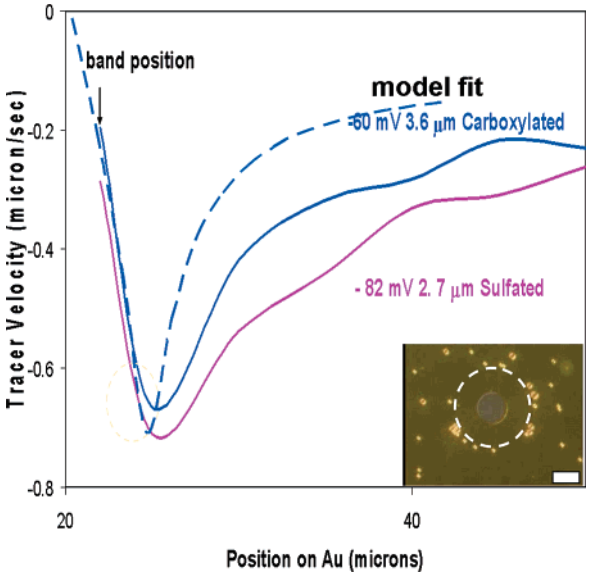

Figure 3. Comparison of experimental tracer velocity $U(r)$ for two types of polystyrene particles to the model. The dashed curve is the model of the tracer velocity for a particle with $\zeta_p = -82$ mV and $\zeta_w = -20$ mV, while the two lower solid curves are the data. The model correctly predicts this maximum in tracer velocity just outside the position ($R_{Au,max}$) of the stable band, as well as the same band position (r_{crit}) for the particles despite the fact that they have different ζ potentials. The upper solid curve is for the carboxylated PSL with $\zeta_p = -60$ mV. The tracers have identical buoyancies but different ζ potentials, but they form a band at the same position as predicted by the model. Inset: Image showing pattern formation at same location ($r_{critical}$ on trajectory plot) around the silver disk on the gold surface for 3.6 μm diameter carboxylated and 2.7 μm diameter sulfated polystyrene particles. The scale bar is 20 μm.

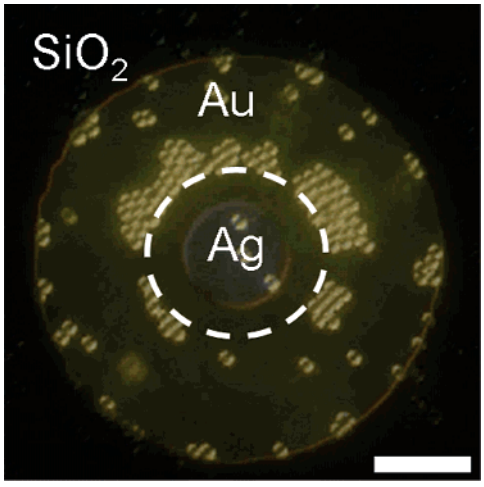

Figure 4. Patterning of silica particles (2.3 μm in diameter) on catalytic surfaces. The image shows band-like formation of silica particles formed around a 20 μm silver disk on a 90 μm gold disk after 0.25 min of observation. Particles appear different colors because of different reflectances of the SiO_2 and gold surfaces. The inner part of the band is highlighted by the white dashed line at about $r = 18$ μm (i.e., 8 μm from the edge of the silver disk). Note the formation of ordered colloidal particles in the band region. The scale bar represents 20 μm.

diameter. Thus, for a 20 μm silver disk, gold disks larger than 72 μm add little additional effect. Calculations show that the band position occurs at $r_{crit} = 0.86R_{Au,mas}$. In the z direction we also find that $E_z = 0$, similar to the field in the radial direction.

Comparison of Experimental Data and Model. To compare our experiments and modeling, we examine the system from Figure 3. This system uses 2.7 μm sulfated polystyrene particles

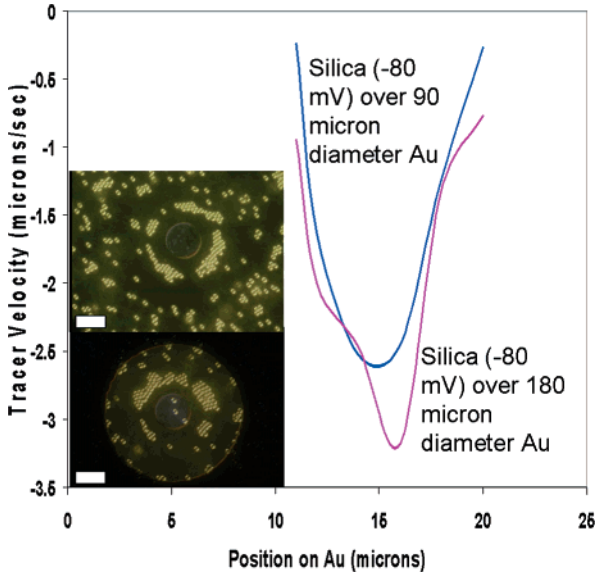

Figure 5. Tracer velocity for silica particles leading to patterning for variations of gold disk size and constant silver disk size (20 μm). The bands form roughly 10 μm from the edge of the silver disk, where the velocity goes to zero. The tracer velocity over the 180 μm gold disk is about 25% higher than that over the 90 μm gold disk (and about 4.6 times higher than the results from Figure 3), and the band positions are only slightly different. Insets show the patterns over the 180 μm diameter gold disk (top) and 90 μm diameter gold disk (bottom). The scale bar is 20 μm.

(ζ potential -82 mV) and 3.6 μm carboxylated polystyrene particles (ζ potential -60 mV) in 0.5% w/w H_2O_2 at a bulk temperature of 23 °C, and we show the observed tracer velocity (**v**) as a function of position from the edge of the silver disk. Our model discussed below uses carboxylated and sulfated polystyrene particle data from Figure 3 but silica particles behave similarly because of similar ζ potential (-80 mV), therefore in Figures 4 and 5 we show patterning for silica particles. The surface below consists of an inner silver disk ($R_{Ag} = 10$ μm), then a sea of gold outside of this.

Two model parameters were fit to the data: The maximum effective gold size ($R_{Au,max}$) and the silver reaction rate (J_{Ag}). $R_{Au,max}$ was fit by setting it equal to the position of maximum tracer velocity outside of the band in Figure 3. J_{Ag} was fit by setting the value of the maximum tracer velocity predicted by the model equal to the tracer velocity for a particle with $\zeta_p = -82$ mV (measured by ZetaPALS). The bulk gold surface ζ potential was estimated to be -20 mV from the literature.[28] We found that $J_{Au} = +6.70 \times 10^{16}$ per m^2·s of H^+, with $J_{Ag} = -8.02 \times 10^{17}$ per m^2·s. This corresponds to $i_{Au} = 10.7$ mA/m^2 and $E_z = +0.49$ V/cm over the gold. In addition, $R_{Au,max} = 36$ μm is the maximum radius of gold disk that makes any significant catalytic contribution for $R_{Ag} = 10$ μm. That is, beyond this point, the reaction becomes rate limiting at the silver. This is supported by the data in Figure 5 where the silver disk is surrounded by a gold disk ($R_{Au} = 90$ or 180 μm), and then SiO_2 (i.e., glass). Thus, when the diameter of the gold disk increases from 90 to 180 μm or larger, the tracer particles' band size and velocities change only slightly. This effective maximum size is consistent with the $V =$ IR voltage drop across the solution, compared with the excess voltage available for the reaction.

The patterns formed in Figures 3−5 occur when $\zeta_p - \zeta_w < 0$. However, if $\zeta_p - \zeta_w > 0$, then the particles simply convect inward. This occurs for positively charged amidine particles, for which both the electrophoretic and the electroosmotic

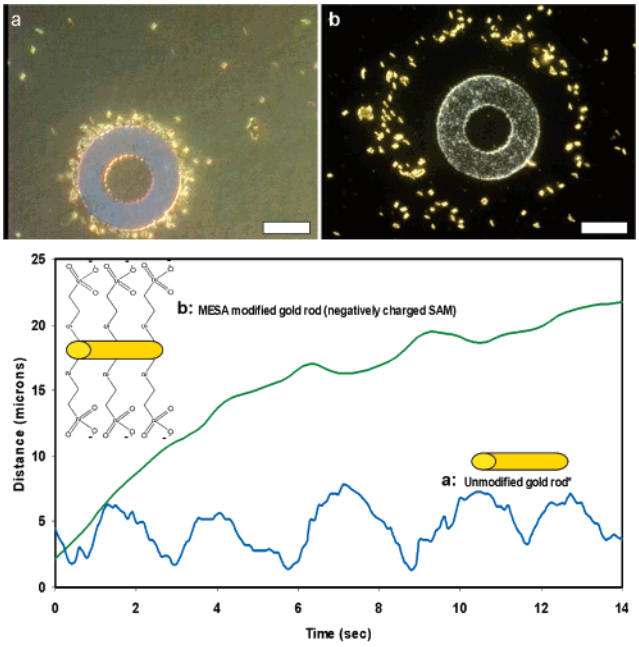

Figure 6. Movement of treated and untreated gold particles around silver annulus on the gold surface. (a) Unmodified gold rods ($\zeta_p = -7$ mV) with $\zeta_p - \zeta_w > 0$, shown crowding around the silver feature (~20 μm in diameter). (b) MESA functionalized gold rods ($\zeta_p = -40$ mV) with $\zeta_p - \zeta_w < 0$, shown giving a pattern. The trajectory plot below the images shows typical convective-like motion of unmodified gold nanorods (labeled a) while MESA-modified gold nanorods move away from the silver disk to form the pattern (labeled b). All tracers are approximately 2−4 μm in length and 380 nm in diameter on a silver-patterned gold surface in a 0.5% w/w aqueous solution of H_2O_2 and observed with 50× objective. The scale bar represents 20 μm.

velocities bring the tracer particles inward. The model predicts that due to a vertical electric field arising from the surface, the amidine particles should be slightly elevated above the gold. This is seen experimentally.

The inward motion also occurs for negatively charged gold nanorod tracers (cylinders 400 nm × 2 μm, $\zeta_p = -7$ mV), since the inward electroosmotic motion dominates the small outward electrophoretic velocity (Figure 6a). In this case the gold surface seems to have a more negative ζ potential than the gold nanorod tracer ($\zeta_p = -7$ mV); we estimate the gold surface to be about −20 mV based on a report in the literature for bulk gold in equilibrium water (pH ~5.5 to 5.7).[28] On the other hand, when we coat the gold nanorods with mercaptoethyl sulfonic acid (MESA), giving $\zeta_p = -40$ mV, the gold nanorods form a stable pattern (Figure 6b). The ζ potentials of bulk gold surfaces modified with SAMs have been measured by Schweiss et al., and were reported to vary depending on the thiol used (e.g., negative or neutral) and our measured results are consistent in direction and magnitude with their results.[28] The electrokinetic model predicts that electroosmosis dominates for unmodified gold nanorod tracers ($\zeta_p - \zeta_w > 0$), and therefore they convect inward.

The untreated gold nanorods form a type of band at the silver−gold edge, and they also exhibit a cyclic convective motion. This occurs because the inward-moving fluid must move upward due to fluid continuity. The fluid carries the gold particles vertically with itself, and then the fluid carries the gold particles slightly outward. Gravity then pulls the particles back down (Figure 6a), where they start the cycle again. On the other hand, for MESA-modified gold nanorod tracers ($\zeta_p - \zeta_w < 0$), electrophoresis dominates and therefore they pattern (Figure 6b). Trajectory plots of tracer motion clearly distinguish the behavior exhibited by unmodified gold nanorods versus modified MESA-modified gold nanorods (see the Supporting Information). Images in Figure 6 show silver annulus on gold surface; the difference in color is due to different microscope settings because images were taken at different times. Table 1 summarizes the measured tracer ζ potentials, sizes, batch number, and observed behavior, highlighting the change from pattern formation to convection for various $\zeta_p - \zeta_w$.

Silica-coated gold rods behave similarly to 2.3 μm silica particles (not shown), forming a pattern around the silver feature. Silica-coated gold rods prepared via the Stober process[29] were used to compare with self-assembled monolayer (MESA) modified gold rods (Figure 6b). The silica coating provided an alternative means of imparting a negative charge to gold nanorods for comparison to MESA modified gold nanorods.

Measuring Reaction Kinetics in Situ. We have previously estimated the electric field strength and reaction rates in H_2O_2 micropump systems from current measurements using interdigitated arrays of gold and silver microelectrodes spaced 10 μm apart on glass.[1] We can also estimate the E field by comparing tracer velocities for two different particles over a gold surface, allowing us to fit the model for the surface ζ potential and the electric field in the system. We now present a third method for measuring the E field. This more direct method is shown schematically in Figure 7.

As Figure 7 shows, our setup allows us to *apply* an external E field while observing the fluid flow created by the catalytic reaction. We measured currents (i) associated with applied voltages and calculated E fields by using Ohm's law:

$$E = \frac{i}{kA} \tag{44}$$

where k is the conductivity of the solution (units 1/Ω·m or S/m), and A is the cross sectional area of the fluid cell (diameter = 8 mm in length by 120 μm in height). After assembling the cell shown in Figure 7, we observed the catalytically generated

TABLE 1: Tracer Particle ζ Potentials in pH 5.7 Equilibrium Water

tracer	ζ potential (mV)[a]	size (micrometers)	lot/batch no.	convection or patterning (C/P)
silica[b]	−80	0.97, 2.3, 5.6	L000801A, L99102A, L001215A	P
sulfated polystyrene[c]	−82	2.3	537345	P
carboxylated polystyrene[c]	−60	3.1	523679	P
carboxy-sulfate polystyrene[c]	−40	1.0	467739	P
MESA gold nanorods[d]	−40	0.4 × 2.0	synthesized	P
gold nanorods[e]	−7	0.4 × 2.0	synthesized	C
amidine polystyrene[f]	40	2.0	A37325	C

[a] All ζ potentials were measured by ZetaPALS. [b] The silica tracers were from Bangs Lab. [c] Most polystyrene particles were from Polysciences Inc. [d] The MESA-modified (alkane-thiol SAM) gold had a much greater magnitude of ζ_p than untreated gold, consistent with ζ_p reported for planar thiol-modified gold surfaces in the literature.[28] [e] The bare gold particles had fairly consistent ζ_p, acting similarly to dielectric particles as previously discussed in the literature.[30] [f] The amidine polystyrene particles were from Interfacial Dynamics.

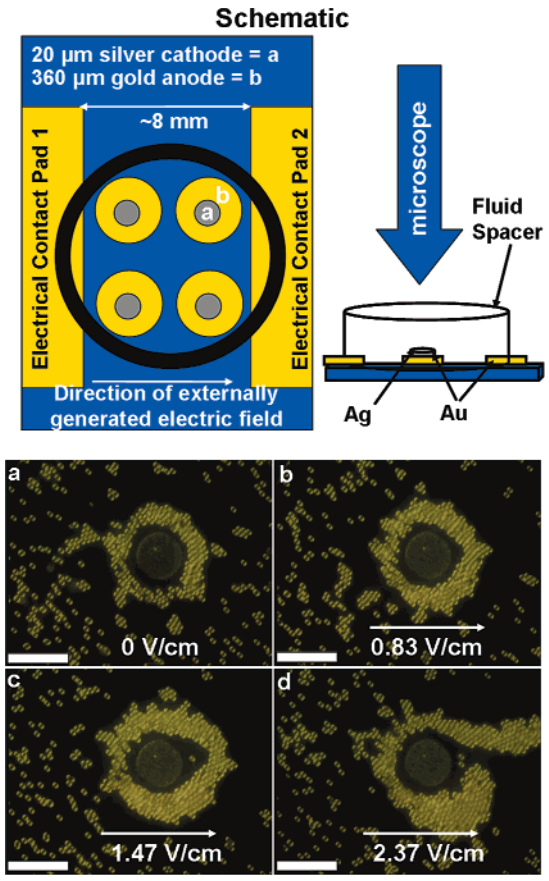

Figure 7. Measurement of the electric field in our system. (top schematic) The design used to measure the catalytically generated *E* field. A voltage is applied to Contact Pad 1. The wires to the pads are isolated from the solution by a fluid gasket to avoid corrosion. The catalysts (silver on gold) are inside the gasket. Also shown is a cross-section of the system with the thickness of each metal shown, including the gold anode, the electrical contact pads, the silver cathode, and the fluid gasket (not drawn to scale). (a) Silica tracers, 2.3 μm in diameter on a surface with a 20 μm silver disk on a 180 μm diameter disk with no applied voltage. (b) Same surface and tracers after applying 0.83 V/cm. (c) Same surface and tracers after increasing the applied field to 1.47 V/cm. Notice the distortion of the ring around the silver. (d) The applied field of 2.37 V/cm is now stronger than the catalytically generated field, causing the pattern to break.

patterning or convection before applying an external voltage. Then we sequentially increased the externally applied voltage, perturbing the pattern, until the pattern broke. The external field is approximately equivalent to the catalytically generated field at this point for highly negative tracers (Figure 7d). For less negatively charged or positively charged tracers that exhibit convective movement, the applied field is approximately equal to the catalytically generated field when the particles stop "flipping" in a convective-like manner. Figure 7a−d illustrates this approach for negatively charged silica tracers.

In Figure 7, the external field causes particles to move from left to right (toward the positive electrode). The externally applied field did not appear to cause any irreversible effects on the system, as confirmed by complete restoration of the catalyst generated pattern (similar to Figure 7a) when the field is turned off. Particles do not move over the silver disk even at high applied fields, since the *E* field over the silver disk is quite strong and pushes the particles outward from itself. We see this in our experiments, and thus we measured the effect of the external field by monitoring the right side of the silver disk.

We ran experiments for five gold surfaces with different

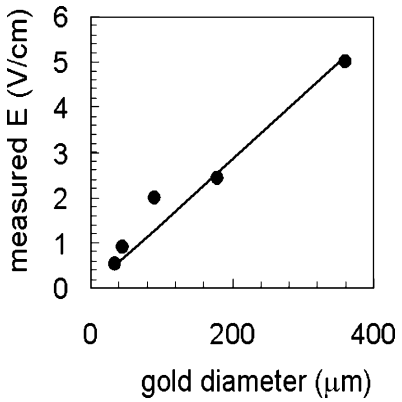

Figure 8. The measured *E* field as a function of the diameter ($2R_{Au}$) of the actual gold disk (not $R_{Au,max}$) for 2.3 μm silica particles. The fit shows that $E = (0.0284 \pm 0.0052)R_{Au}$, with a 95% confidence interval.

diameters (35 to 360 μm in diameter) and measured the applied field needed to break the patterning or stop convection, depending on the particle type. An ellipse should form with an applied *E* field, which is consistent with the patterns observed. We found that applied *E* fields were on the order of the estimates we obtained previously with interdigitated arrays of silver and gold electrodes, and with our calculations based on tracer velocities. Furthermore, we found an approximately linear trend in required *E* field to break the ring, as a function of the gold catalytic disk diameter (Figure 8). Data in Figure 8 were obtained with 2.3 μm silica particles but other negatively charged particles were observed to give similar trends. In addition, we observed a linear trend with velocity for tracers that exhibited convection. Thus, while the band position appears to asymptote as the diameter of the gold disk increases, the *E* field and tracer velocity increases. This suggests that future studies will require a more detailed reaction kinetics model in place of eq 32, which is an input to the present model.

Conclusions

We have derived a predictive electrokinetic model describing tracer motion in the presence of catalytic decomposition of H_2O_2 on gold and silver catalysts. The model has several justifiable assumptions in it, and it predicts key features like a patterned band of particles for $\zeta_p - \zeta_w < 0$, a maximum convective velocity just outside the ring, inward convection of tracer particles for $\zeta_p - \zeta_w > 0$, and the correct direction of the tracer velocities. The model supports the observations by Paxton et al. for the electroosmosis-dominated convection of tracers on platinum/gold interdigitated miroelectrodes in H_2O_2.[18]

By combining the experimental data with an interpretation using the electrokinetic model, we are also able to measure in situ the electrochemical reaction rates on the gold and silver. We found that while the silver has a higher reaction rate per unit area, due to its small size it becomes the rate-limiting catalyst after the size of gold exceeds $R_{Au,max}$. For one silver disk with a diameter of 20 μm, the maximum gold disk diameter over which significant reaction occurred was about 70 μm. The rate of reaction was fit to date to be $J_{Au} = 6.7 \times 10^{16}$ per m^2·s of H^+ and $J_{Ag} = -8.02 \times 10^{16}$ per m^2·s. Some variation does exist from one catalytic system to another, even when similar steps were taken during fabrication.

The electrokinetic model discussed could be easily modified for broken symmetry systems, currently under investigation in our lab. Second, this electrokinetic model could be applied to redox systems other than hydrogen peroxide. One such system could be the bioelectrochemical propulsion of carbon microfibers

via self-generated electric fields, from an enzymatically driven reaction, reported by Mano and Heller.[31] Finally, this work continues to expand the possibilities of asymmetric catalysis in generating autonomous movement by using surfaces as motors. Using surfaces as motors may find practical applications in microfluidic channel networks.

Acknowledgment. We thank Vincent Crespi, Walter Paxton and Jeffrey Catchmark, for insightful discussions, and James Sioss for the first batch of silica coated gold nanorods. Financial support for this project was made possible by the Penn State Materials Research Science and Engineering Center (NSF-MRSEC, DMR-021362).

Supporting Information Available: X-ray photoelectron spectroscopy data of MESA modified gold surface before and after exposure to H_2O_2. This material is available free of charge via the Internet at http://pubs.acs.org.

References and Notes

(1) Kline, T. R.; Paxton, W. F.; Wang, Y.; Velegol, D.; Mallouk, T. E.; Sen, A. *J. Am. Chem. Soc.* **2005**, *127*, 17150−17151.

(2) Reuss, F. F. *Mem. Soc. Imperiales Naturalistes Moskou* **1809**, *2*, 327−336.

(3) Dukhin, S. S.; Derjaguin, B. V. *Electrokinetic Phenomena*; Surface Colloid Science, Vol. 7; Matijevic, E., Ed.; Wiley: New York, 1974.

(4) O'Brien, R. W.; White, L. R. *J. Chem. Soc., Faraday Trans. 2* **1978**, 74, 1607−1626.

(5) Hunter, R. J. *Zeta Potential in Colloid Science: Principles and Applications*; Academic Press: New York, 1981.

(6) Teubner, M. *J. Chem. Phys.* **1982**, *76*, 5564−5573.

(7) Anderson, J. L. *Annu. Rev. Fluid Mech.* **1989**, *21*, 61−99.

(8) Solomenstev, Y.; Bohmer, M.; Anderson, J. L. *Langmuir* **1997**, *13*, 6058−6068.

(9) Solomenstev, Y.; Guelcher, S. A.; Bevan, M.; Anderson, J. L. *Langmuir* **2000**, *16*, 9208−9216.

(10) Mishchuk, N. A.; Barany, S.; Tarovsky, A. A. *Colloids Surf., A* **1998**, *140*, 43−51.

(11) Trau, M.; Sankaran, S.; Saville, D. A.; Aksay, I. A. *Langmuir* **1995**, *11*, 4665−4672.

(12) Isambert, H.; Ajdari, A.; Viovy, J. L. *J. Prost. Phys. Rev. Lett.* **1997**, *78*, 971−974.

(13) Ristenpart, W. D.; Aksay, I. A.; Saville, D. A. *Phys. Rev. Lett.* **2003**, *90*, 128303−12830.1.

(14) Abe, M. Y. A.; Orita, M.; Ohkubo, T.; Sakai, H.; Momozwaw, N. *Langmuir* **2004**, *20*, 7021−7026.

(15) Hayward, R. C.; Saville, D. A.; Aksay, I. A. *Nature* **2000**, *404*, 56−59.

(16) Paxton, W. F.; Kistler, K. C.; Olmeda, C. C.; Sen, A.; St. Angelo, S. K.; Cao, Y.; Mallouk, T. E.; Lammert, P. E.; Crespi, V. H. *J. Am. Chem. Soc.* **2004**, *126*, 13242−13231.

(17) Kline, T. R.; Paxton, W. F.; Mallouk, T. E.; Sen, A. *Angew. Chem., Int. Ed.* **2004**, *44*, 744−746.

(18) Paxton, W. F.; Baker, P. T.; Kline, T. R.; Wang, Y.; Mallouk, T. E.; Sen, A. *J. Am. Chem. Soc.* Submitted for publication.

(19) St. Angelo, S. K.; Waraksa, Ch. C.; Mallouk, T. E. *Adv. Mater.* **2003**, *15*, 400−402.

(20) Martin, B. R.; St. Angelo, S. K.; Mallouk, T. E. *Adv. Funct. Mater.* **2002**, *12*, 759−765.

(21) Keh, H. J.; Anderson, J. L. *J. Fluid Mech.* **1985**, *153*, 417−439.

(22) Russel, W. B.; Saville, D. A.; Schowalter, W. R. *Colloidal Dispersions*; Cambridge University Press: New York,1989; with corrections 1991.

(23) Prieve, D. C. *Colloids Surf., A* **2004**, *250*, 67−77.

(24) Bard, A. J.; Faulkner, L. R. *Electrochemical Methods*: *Principles and Applications*, 2nd ed.; John Wiley and Sons: New York, 2001.

(25) Jackson, J. D. *Classical Electrodynamics*, 3rd ed.; Wiley: New York, 1999.

(26) Anderson, J. L. *J. Colloid Interface Sci.* **1985**, *105*, 45−54.

(27) Giesbers, M.; Kleijn, J. M.; Cohen, S. M. A. *J. Colloid Interface Sci.* **2002**, *248*, 88−95.

(28) Schweiss, R.; Welzel, P. B.; Werner, C.; Knoll, W. *Langmuir* **2001**, *17*, 4304−4311.

(29) Yin, Y. L. Y.; Sun, Y.; Xia, Y. *Nano Lett.* **2002**, *2*, 427−430.

(30) Harrison, J. T.; Elton, G. A. H. *J. Chem. Soc.* **1959**, 3838−3843.

(31) Mano, N.; Heller, A. *J. Am. Chem. Soc.* **2005**, *127*, 11574−11575.